China Ocean Eng., 2022, Vol. 36, No. 6, P. 880–893
DOI: https://doi.org/10.1007/s13344-022-0079-7, ISSN 0890-5487
http://www.chinaoceanengin.cn/ E-mail: coe@nhri.cn

Investigation on Effects of Mooring Line Fractures and Connector Failures for A Hybrid Modular Floating Structure System

LIU Ya-qiong[a], REN Nian-xin[b], OU Jin-ping[a, *]

[a] School of Civil and Environmental Engineering, Harbin Institute of Technology (Shenzhen), Shenzhen 518055, China

[b] College of Civil Engineering and Architecture, Hainan University, Haikou 570228, China

Received August 22, 2022; revised October 17, 2022; accepted November 8, 2022

Abstract

The present work reports a Hybrid Modular Floating Structure (HMFS) system with typical malfunction conditions. The effects of both fractured mooring lines and failed connectors on main hydrodynamic responses (mooring line tensions, module motions, connector loads and wave power production) of the HMFS system under typical sea conditions are comparatively investigated. The results indicate that the mooring tension distribution, certain module motions (surge, sway and yaw) and connector loads (M_z) are significantly influenced by mooring line fractures. The adjacent mooring line of the fractured line on the upstream side suffers the largest tension among the remaining mooring lines, and the case with two fractured mooring lines in the same group on the upstream side is the most dangerous among all cases of two-line failures in view of mooring line tensions, module motions and connector loads. Therefore, one emergency strategy with appropriate relaxation of a proper mooring line has been proposed and proved effective to reduce the risk of more progressive mooring line fractures. In addition, connector failures substantially affect certain module motions (heave and pitch), certain connector loads (F_z and M_y) and wave power production. The present work can be helpful and instructive for studies on malfunction conditions of modular floating structure (MFS) systems.

Key words: Hybrid Modular Floating Structure (HMFS) system, mooring line fractures, connector failures, hydrodynamic responses, emergency strategy

Citation: Liu, Y. Q., Ren, N. X., Ou, J. P., 2022. Investigation on effects of mooring line fractures and connector failures for a hybrid modular floating structure system. China Ocean Eng., 36(6): 880–893, doi: https://doi.org/10.1007/s13344-022-0079-7

1 Introduction

Modular Floating Structure (MFS) systems have attracted significant attention in development and utilization of marine space and resources for diverse applications in conceptual or practical ways, such as fish farm (Berstad et al., 2004), floating performance stage (Nguyen et al., 2020), floating airfield (Suzuki, 2005), floating pier (Jung et al., 2020), floating oil storage facilities (Chuyen, 2009), floating wind farm (Manabe et al., 2008), floating city (Wang and Tay, 2011), etc. MFS systems usually refer to a kind of large floating structure system assembled of a certain number of single modules with reasonable size by appropriate connection types. Therefore, connection systems and mooring systems are the most important components of MFS systems (Liu et al., 2021).

For ensuring personnel safety and function realization, it is essential to apply appropriate mooring methods for stabilizing modules' positions within safe ranges (Lian et al., 2020; Wang and Wang, 2015). Chain mooring methods, including taut-wire mooring systems (TMS) and catenary mooring systems (CMS), are commonly used for MFS systems in consideration of its wide adaptability to water depth and its convenience for installation, expansion and removal (Liu et al., 2021; Lian et al., 2018). It is probable for an MFS system to suffer from mooring line fractures during long-term service due to various possible factors, such as design deficiency, installation error, improper material and fabrication, corrosion and aging, fatigue and ultimate fracture, etc (Ma et al., 2013; Ahmed et al., 2016). Mooring line fractures usually lead to significant position shift of floating platforms (Kim et al., 2014). More seriously, floating platforms can probably lose stability, overturn and even collide with other floating bodies nearby (Fontain et al., 2014; Ma et al., 2020). Therefore, it is of great significance to evaluate

Foundation item: This research was financially supported by Shenzhen Science and Technology Program (Grant No. KQTD20210811090112003) and the National Natural Science Foundation of China (Grant No. 52161041).

*Corresponding author. E-mail: oujinping163@163.com

the impact of potential mooring line fractures in the design stage for prevention and repairing.

Cheng et al. (2021) conducted time-domain simulations to investigate the effects of mooring line breakage on structural responses (mooring line tension distribution and buoy displacement) of grid moored fish farms. Qiao et al. (2021) evaluated the transient responses (mooring line tension and vessel motion) of a Floating Production Storage and Offloading (FPSO) with various mooring failure scenarios under different environmental conditions through a series of time-domain numerical analysis based on ANSYS AQWA. Yang et al. (2021) investigated the influences of a sudden mooring breakage on dynamic responses (rotor motions, platform motions and the remaining mooring system) of a 5 MW barge-type Floating Offshore Wind Turbine (FOWT) under various operating states through a coupling framework (F2A) based on FAST and AQWA. Bae et al. (2017) adopted an analysis tool combining CHARM3D and FAST to analyze the performance changes of a 5MW semi-sub FOWT due to breakage at different mooring lines for an aero-servo-elastic-mooring fully coupled dynamic system. Malayjerdi et al. (2016) conducted the dynamic analysis of a tension leg platform (TLP) in intact and damaged tendon conditions, including performances of stability, motion stiffness and motion responses. Ren et al. (2022) carried out dynamic analysis of tendon-failure influences on a multi-column TLP floating offshore wind turbine. Li et al. (2018) proposed a coupled aero-hydro-elastic time-domain numerical model for investigating an OC3 Hywind SPAR-type FOWT in various scenarios with different fractured mooring lines and shutdown strategies, mainly considering the platform motion, mooring line tension and power generation performance.

Most of the above-mentioned studies focus on the effects of mooring failures on a single floating platform (FPSO, FOWT, TLP, etc.) under typical irregular wave conditions. The investigated hydrodynamic responses mainly include mooring tensions and platform motions. To the authors' best knowledge, studies about the influence of mooring failures on MFS systems are rare. In fact, the contents of hydrodynamic responses of MFS systems are more extensive than those of a single floating platform (Liu et al., 2022). In addition, considering that sudden mooring line fracture may occur in any wave conditions (even mild wave conditions) due to material aging or fatigue, the effects of different wave levels should be investigated under regular waves with different wave periods, which is lacking in the existing research. Furthermore, the connector failure between modules is also a significant malfunction type for MFS system, which should be laid stress on for ensuring integrity and continuity of MFS systems. However, it is rarely investigated in existing studies.

The present work reports a Hybrid Modular Floating Structure (HMFS) system with typical malfunction conditions. The HMFS system consists of hybrid modules connected in longitudinal and transverse directions by two connection types. It is moored to the sea bed with multiple catenary mooring lines. The effects of different quantities or locations of both fractured mooring lines and failed connectors on the main hydrodynamic responses (mooring line tensions, module motions, connector loads and wave power production) of the HMFS system under typical sea conditions are comparatively investigated through time-domain numerical simulations based on ANSYS AQWA. In addition, one emergency strategy of increasing the relaxation of proper mooring lines has been proposed and analyzed for reducing the risk of more progressive mooring line fractures.

2 Numerical model

The numerical hydrodynamic model (wet surface model) of the HMFS system based on ANSYS AQWA is presented in Fig. 1. Since module motions are far greater than module deformation due to relatively small module size, all modules are considered as rigid bodies. In addition, flexible connectors almost bear all the "deformation" (Kim et al., 2007). Therefore, the Rigid Module and Flexible Connector (RMFC) method is applied for time-domain analysis of the HMFS system (Du and Ertekin, 1991; Chen et al., 2021). The hydrodynamic coupling effect of multi-body and mechanical coupling effect of connectors are taken into consideration.

2.1 Motion equations of the HMFS system (time domain)

Based on Newton's Second Law, the time-domain motion equation of the HMFS system can be expressed as:

$$\sum_{j=1}^{6N} M_{kj}\ddot{\xi}_j(t) = F_{k,\mathrm{wave}}(t) + F_{k,\mathrm{con}}(t) + F_{k,\mathrm{PTO}}(t) + F_{k,\mathrm{m}}(t) + F_{k,\mathrm{fender}}(t), \quad (1)$$

where N represents the total number of modules; $M_{kj}(t)$ is the generalized mass matrix coefficient; $\ddot{\xi}_j(t)$ is the motion acceleration of a certain degree of freedom (DOF) of a module. The external forces of modules mainly include the wave force $F_{k,\mathrm{wave}}$, the connection spring force $F_{k,\mathrm{con}}$, the connection Power Take-Off (PTO) damping force $F_{k,\mathrm{PTO}}$, the mooring force $F_{k,\mathrm{m}}$, and the fender force $F_{k,\mathrm{fender}}$.

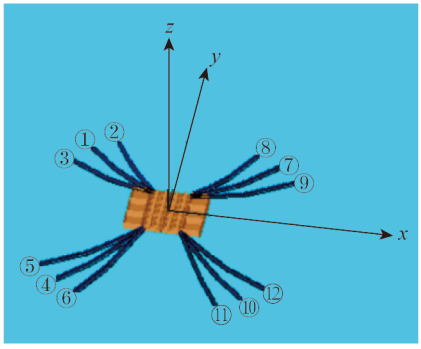

Fig. 1. Hydrodynamic numerical model of the HMFS system.

2.2 Wave force

For MFS systems, the total wave force $F_{k,\mathrm{wave}}$ includes hydrostatic restoring force $F_{k,\mathrm{HS}}$, wave radiation force $F_{k,\mathrm{R}}$ and wave excitation force $F_{k,\mathrm{EX}}$ (Faltinsen, 1990). The hydrostatic restoring force $F_{k,\mathrm{HS}}$ can be expressed as:

$$F_{k,\mathrm{HS}} = -C_{kj}\xi_j(t), \tag{2}$$

where C_{kj} is the hydrostatic force coefficient. $\xi_j(t)$ indicates the displacement of the j-th direction.

The radiation force can be expressed as (Cummins, 1962):

$$F_{k,\mathrm{R}}(t) = -\sum_{j=1}^{6N}\left[m_{kj}\ddot{\xi}_j(t) - \int_{-\infty}^{t}\dot{\xi}_j(\tau)K_{kj}(t-\tau)\mathrm{d}\tau\right], \tag{3}$$

where ρ is the fluid density. m_{kj} and $K_{kj}(t)$ are the additional mass coefficient and delay function coefficient, respectively. $\dot{\xi}_j(\tau)$ indicates the velocity of the j-th direction.

The delay function can be expressed as:

$$K_{kj}(t) = \frac{2}{\pi}\int_0^{\infty} B_{kj}(\omega)\cos(\omega t)\mathrm{d}\omega, \tag{4}$$

where $B_{kj}(\omega)$ is the radiation damping derived through frequency domain analysis.

2.3 Connection force

The connection spring force $F_{k,\mathrm{con}}$, the connection PTO damping force $F_{k,\mathrm{PTO}}$ and the fender force $F_{k,\mathrm{fender}}$ of the k-th direction can be expressed as (Liu et al., 2022):

$$F_{k,\mathrm{con}}(t) = \sum_{j=1}^{6N}\varphi_{kj}K_{kj}\delta\left[\xi_k(t),\xi_j(t)\right]; \tag{5}$$

$$F_{k,\mathrm{PTO}}(t) = \sum_{j=1}^{6N}\varphi_{kj}C_{kj}v\left[\xi_k(t),\xi_j(t)\right]; \tag{6}$$

$$F_{k,\mathrm{fender}}(t) = \begin{cases} \sum_{j=1}^{6N}\varphi_{kj}K_{kj}^{\mathrm{f}}\left|\delta'[\xi_k(t),\xi_j(t)]+4\right| & \text{if } \delta'[\xi_k(t),\xi_j(t)] \leqslant -4 \text{ m} \\ 0 & \text{if } \delta'[\xi_k(t),\xi_j(t)] > -4 \text{ m} \end{cases} \tag{7}$$

where K_{kj},C_{kj} and K_{kj}^{f} are the connection spring stiffness coefficient, the connection PTO damping coefficient and the fender stiffness coefficient, respectively. $\delta\left[\xi_k(t),\xi_j(t)\right]$ and $v\left[\xi_k(t),\xi_j(t)\right]$ are the relative displacement and the relative velocity of connection points, respectively. The fender is simplified as unidirectional linear spring, and $\delta'\left[\xi_k(t),\xi_j(t)\right]$ is the relative displacement of the fenders between two adjacent modules. φ_{kj} is a kind of matrix coefficient that the value is one when $\xi_k(t)$ and $\xi_j(t)$ are presented for two connected modules respectively, otherwise, it is set to be zero.

2.4 Wave energy power

The wave energy power $P_{\mathrm{w}}(t)$ of the outermost connectors which are equipped with linear pitch PTO damping systems can be expressed as (Ren et al., 2020):

$$P_{\mathrm{w}}(t) = M_{\mathrm{PTO}}^2(t)\Big/K_{\mathrm{p}}, \tag{8}$$

where M_{PTO} is the pitch damping torque and K_{p} is the PTO damping coefficient.

For solving the motion equation of the HMFS system, the additional mass matrix, radiation damping matrix, hydrostatic force matrix and wave excitation force matrix should be firstly obtained through frequency domain analysis (AQWA Line). The mooring motion equation is established based on the lumped mass method and solved by Finite Difference Method (FDM) (Wang et al., 2019). Combined with the mooring motion equations, the motion equation of the HMFS system is solved through AQWA Drift (irregular wave) or Naut (regular wave) which are based on Newmark-Beta numerical method (Newmark, 1959), and time domain results of the main hydrodynamic responses can be obtained.

3 Description of the HMFS system

This study focuses on a novel hybrid modular floating structure (HMFS) system which consists of six outermost box-type modules and six inner semi-sub modules (Fig. 3) (Liu et al., 2021). Based on different hydrodynamic characteristics, box-type modules are designed as breakwaters and Wave Energy Converter (WEC) modules (Cheng et al., 2022; Li et al., 2022), and semi-sub modules are designed as the main production and living modules. The HMFS system is arranged considerately in a way that the transverse direction is consistent with wave direction of the highest occurrence probability (the incident wave angle of 0°) (Liu et al., 2022). The box-type modules are only set on the upstream and the downstream side mainly due to ship berthing, goods transportation and cost-efficiency. Module dimensions are primarily selected in consideration of construction, transportation and installation. The main dimensions and properties of the two module types are given in Table 1. The gap distance of adjacent modules is preliminarily selected to be 4 m mainly considering connector dimension, module dimension, module motions and resonance effect of narrow slots (Miao et al., 2000). Modules are marked as Mi and connectors are marked as $\mathrm{C}_{i,j}$ (between Mi and Mj), for example, $\mathrm{C}_{5,6}$ is the connector between M5 and M6, and $\mathrm{C}_{6,7}$ is the connector between M6 and M7.

Sketches of two connection types arranged in different positions are shown in Fig. 2. Pitch hinges with additional linear pitch PTO damping systems (essential component of WECs) are arranged between box-type and semi-sub modules (Fig. 2a). Ball joints with linear springs are arranged between adjacent semi-sub modules (Fig. 2b). The pitch PTO damping coefficient (K_{p}) is preliminarily set as 3×10^9 Nms/rad for all outermost connectors, and the spring stiffness coefficient (K_{s}) for roll, pitch and yaw are prelimi-

Table 1 Main design parameters for two module types

Parameters		Semi-sub module	Box-type module
Water depth (m)		40	40
Length, width, height (m)		40, 40, 28	40, 40, 28
Column	Section radius, height, spacing (m)	7, 12, 6	
Pontoon	Length, width, height (m)	40, 40, 8	
	Draft (m)	14	14
	Z_{CoG} (m)	0 (at MWL)	0 (at MWL)
	Weight (t)	16890	22960
	Displacement (t)	16890	22960
	R_{xx}, R_{yy}, R_{zz} (m)	16, 16, 17	15, 15, 16

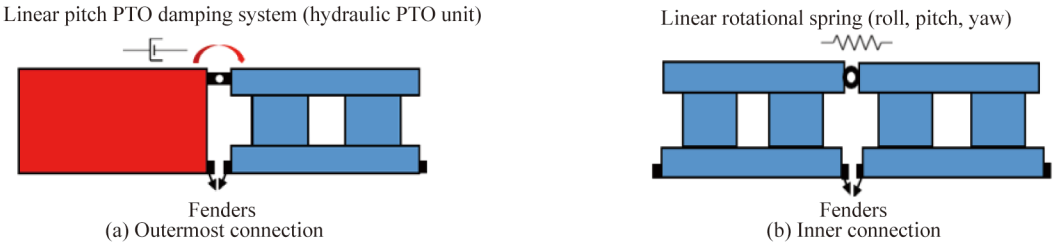

Fig. 2. Sketches of two connection types.

narily set as 1×10^9 Nm/rad for all inner connectors. In addition, modules are all provided with side fenders for fear of potential collisions. The thickness of the fender is 0.4 m and the stiffness is 3.6×10^6 N/m. The initial distances between the contact points and contact planes are all 3.6 m.

In order to keep the HMFS system in given location ranges for stability and safety, a catenary mooring system consisting of 12 mooring lines (3×4 groups) (Fig. 1 and Fig. 3) is preliminarily designed based on wave conditions of selected sea site. The mooring system is symmetrical with respect to the *x*-axis and *y*-axis. Four corner semi-sub modules are separately anchored to the seabed through three mooring lines located at 15° apart. The pretension of four mooring lines is about 1.42 MN. All mooring lines are provided with the same dimensions and properties, as listed in Table 2. Coordinate information of fairlead points and anchor points of a group is presented in Table 3, and those of the other three groups can be inferred due to symmetry.

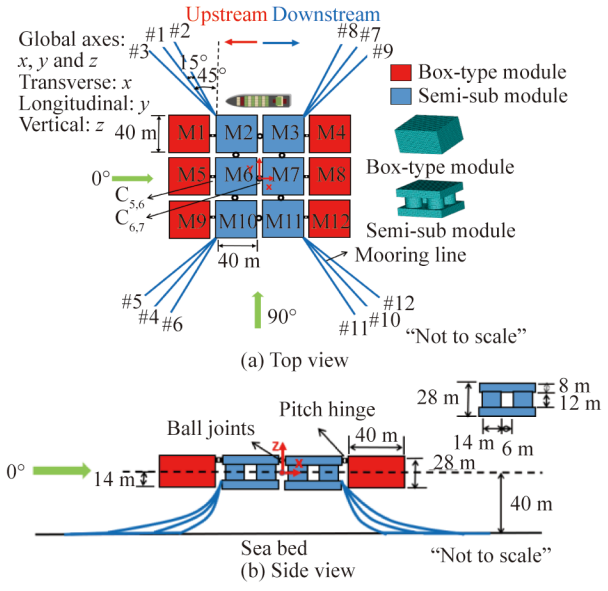

Fig. 3. Sketch of the proposed HMFS system.

Table 2 Detailed information of mooring lines

Properties	Value
Total length (m)	290
Equivalent cross-section area (m^2)	0.0156
Dry weight (kg/m)	171.9
Extensional stiffness (MN)	850
Break strength (MN)	8.5

Table 3 Coordinate information of fairlead points and anchor points

Mooring lines	Fairlead point	Anchor point
#1	(−42, 64, −6)	(−242, 264, −40)
#2	(−42, 64, −6)	(−183.4, 308.9, −40)
#3	(−42, 64, −6)	(−286.9, 205.4, −40)

4 Numerical results

This paper mainly investigates the influence on hydrodynamic responses of the HMFS system due to potential mooring line fractures and connector failures based on ANSYS AQWA. Computational convergence has been checked.

4.1 Effects of one single mooring line fracture under regular waves

4.1.1 *Mooring line tensions*

The mooring tension distribution in intact state under

regular waves with different wave periods (H=2 m, incident wave angle of 0°) are presented in Fig. 4. Upstream-side (#4, #5, #6) and downstream-side mooring lines (#10, #11, #12) are selected as representative objects due to symmetry. Some qualitative comments can be made based on Fig. 4. Tension of mooring lines in the same group shows a similar trend with the wave period increasing. It seems that the tension is less sensitive to wave periods for all mooring lines when the wave period is less than 12 s. However, mooring line tensions increase sharply in the wave period of 12 s especially for upstream-side mooring lines. It may be due to the reason that the pre-tension is high enough to resist the changes of wave force induced by wave period increasement in lower wave period range. Therefore, the wave period of 12 s calls for special attention in consideration of sharp increasement of mooring line tensions. In addition, considering larger mooring line tension, it is noted that the middle line (#4 and #10) for each mooring group should be focused on when the wave period is less than 12 s, and the focus should be shifted to outermost mooring lines (#5 and #12) after wave period of 12 s, especially for the upstream-side line #5.

In light of the possibility of mooring line fracture due to larger tension, mooring lines #5 and #12 are selected as the assumed fracture objects for comparison. The sudden mooring line fracture is set at the same specific instant time for each simulation. Tension variations of representative mooring lines (#4, #10) under regular waves are comparatively presented in Fig. 5. A single mooring line fracture does not lead to trend change of mooring line tensions with varying wave periods at all. In addition, it can be observed that the tensions of remaining mooring lines change when the fracture occurs in different mooring lines. For instance, the fracture of line #5 leads to increase to its adjacent line #6 and decrease to the opposite-side inner line #10 for all wave periods. Similarly, the fracture of line #12 leads to increase to its adjacent line #10 and decrease to the opposite-side inner line #4 for all wave periods.

Fig. 5 also indicates that tension value orders for three mooring scenarios (intact state, line #5 fracture, line #12 fracture) almost remain unchanged under all wave periods. Based on this, changing rates of remaining mooring line tensions for two mooring fracture scenarios compared with intact state under a regular wave (12 s) are shown intuitively in Fig. 6. When the upstream-side line #5 fractures, lines #4 and #6 in the same group show tension increasement by 39.11% and 18.00%, respectively. However, tensions of downstream-side lines #8 and #12 are significantly reduced by 22.52% and 36.57%, respectively. Similarly, when the downstream-side line #12 fractures, tensions of lines #10 and #11 increase by 39.12% and 18.17% respectively, while upstream-side mooring lines #2 and #5 show obvious tension reductions by 22.78% and 36.52%, respectively. Therefore, it can be concluded that tensions of the other two mooring lines which are in the same group with the fractured mooring

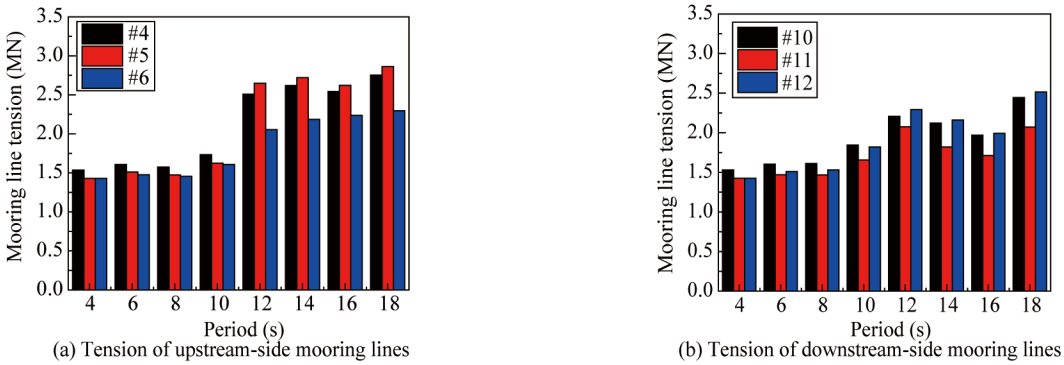

Fig. 4. Mooring line tension distribution in intact state under regular waves.

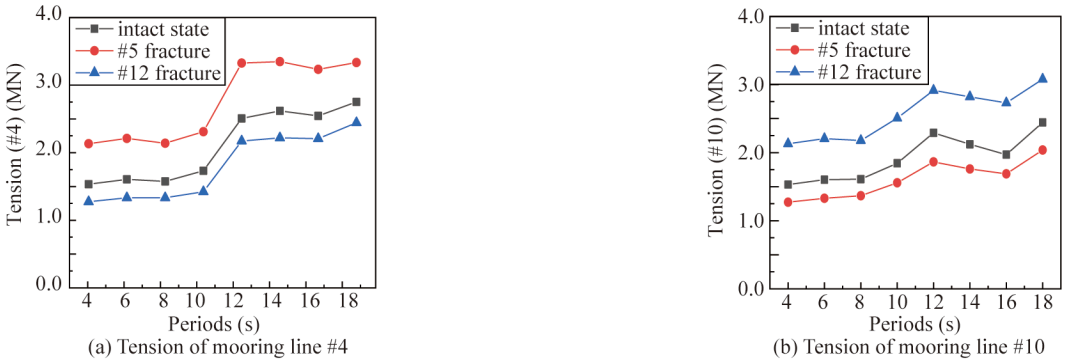

Fig. 5. Mooring line tensions in different mooring scenarios under regular waves.

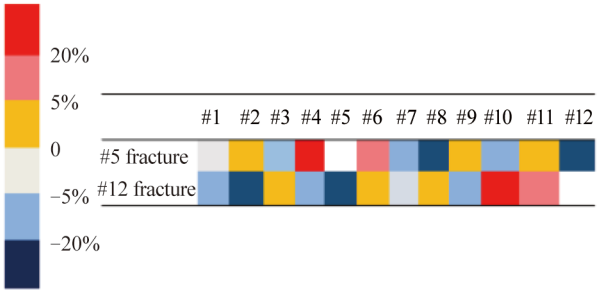

Fig. 6. Mooring line tension changes for two mooring fracture scenarios under the regular wave (12 s).

line both significantly increases, and the tension increase for the adjacent mooring line is much larger. Besides, significant tension reduction usually occurs in certain mooring lines located on the opposite side. It should be noted that special attention should be paid to mooring lines which are in the same group with the fractured line, especially the adjacent mooring line, for preventing progressive fractures in them.

For more insight to the influence of mooring line fractures and grasping the potential mooring fracture risks, the values and locations of the maximum and minimum tensions among all mooring lines for three mooring scenarios under regular waves are investigated. Corresponding results are shown in Fig. 7 and Table 4. It can be seen from Fig.7 that compared with intact state, a single mooring line fracture on either upstream side (line #5) or downstream side (#12) leads to larger maximum mooring tensions and smaller minimum mooring tensions for any regular wave periods. In addition, maximum tensions of the two mooring fracture scenarios are similar in the wave periods below 10 s, while the maximum tensions for the fracture scenario of the upstream-side line #5 is obviously larger than the corresponding values for the fracture scenario of the downstream-side line #12 in wave periods larger than 10 s. In Table 4, for the two fractured mooring scenarios, the location corresponding to the maximum tension keeps on its adjacent mooring line in any wave periods. However, the minimum tension always occurs on the opposite side, and the specific location changes with different wave periods due to mooring line tension redistribution.

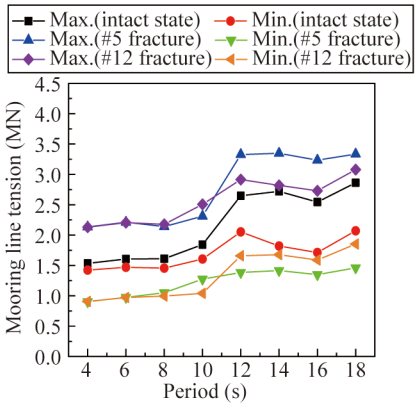

Fig. 7. Maximum and minimum tensions among all mooring lines for three mooring scenarios under regular waves.

4.1.2 *Module motions*

In order to investigate the influence of a single mooring fracture on module motions, a representative module M10 which is connected to the fractured mooring line is selected as the object. Fig. 8 shows comparative results of equilibrium positions of M10 for three mooring scenarios under regular waves with different wave periods.

The equilibrium position of each degree of freedom (DOF) changes for different wave periods and different mooring scenarios. It may be due to different mooring tension distributions corresponding to various mooring scenarios and wave periods. It can be seen that a single mooring line fracture leads to notable equilibrium position changes in horizontal plane motions (surge, sway and yaw) and minor changes in the other motions (heave, roll and pitch), which is because the mooring lines in this paper are mainly functioned for limiting the horizontal plane motions. The fractured mooring lines on different sides (upstream and downstream) lead to different variation direction of equilibrium positions for surge, sway and yaw. For instance, when the fracture occurs on the upstream-side line #5, M10 drifts to new surge and sway equilibrium positions along the positive direction of x-axis and negative direction of y-axis, respectively. In addition, M10 rotates clockwise around the z-axis to a new yaw equilibrium position. On the contrary, when the downstream-side line #12 fractures, the module moves along reverse directions to its new equilibrium positions for surge, sway and yaw. It is because the fractures of a single mooring line on different sides result in force imbalance in opposite directions. In addition, heave equilibrium positions for the two mooring fracture scenarios are both higher than that of intact state, which is because the restraint of mooring

Table 4 Locations of maximum and minimum mooring line tensions for three mooring scenarios under regular waves

Wave period (s)		4	6	8	10	12	14	16	18
Intact state	Line (Max.)	#1 & #4		#3 & #5					
	Line (Min.)	#8 & #11							
#5 fracture	Line (Max.)	#4							
	Line (Min.)	#12					#8		
#12 fracture	Line (Max.)	#10							
	Line (Min.)	#5					#2		

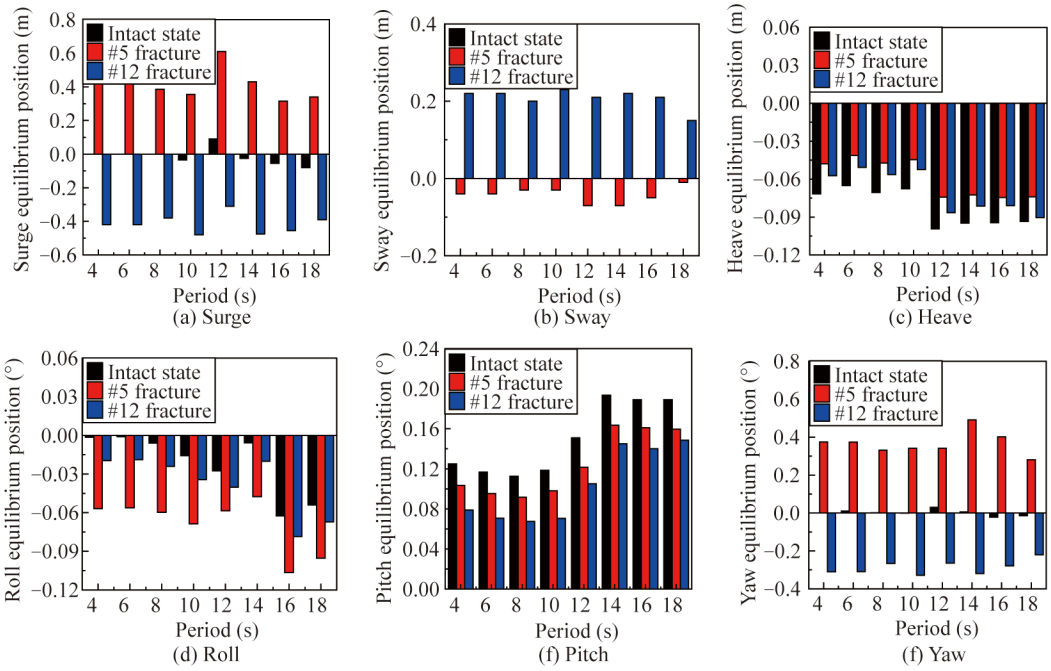

Fig. 8. Equilibrium positions of six DOFs of M10 for three mooring scenarios under regular waves.

lines in the vertical direction is released to a certain extent. There are similar reasons for changes of pitch and roll equilibrium positions.

For more intuitive understanding of module motion variations, time history curves of M10 motions for three mooring scenarios under a regular wave (12 s) are presented in Fig. 9. It indicates that when a single mooring fracture occurs, the module moves reciprocally around new equilibrium positions for six DOFs. Owing to the 0° incident wave, the surge, heave and pitch are in large amplitudes, while the sway, roll and yaw are in relatively small amplitudes.

In addition, motion amplitudes for heave, roll and pitch all change slightly for the two fractured mooring scenarios, which indicates that they are all less sensitive to a single mooring fracture. It is enlightened that when a single mooring line fractures, the motion variations in surge, sway and yaw should be emphatically considered in case of potential module collisions.

4.1.3 *Connector loads*

To better understand the influence of a single mooring fracture on connector loads, results of maximum connector loads of a representative connector $C_{10,11}$ for three mooring scenarios under regular waves are presented in Fig. 10. The

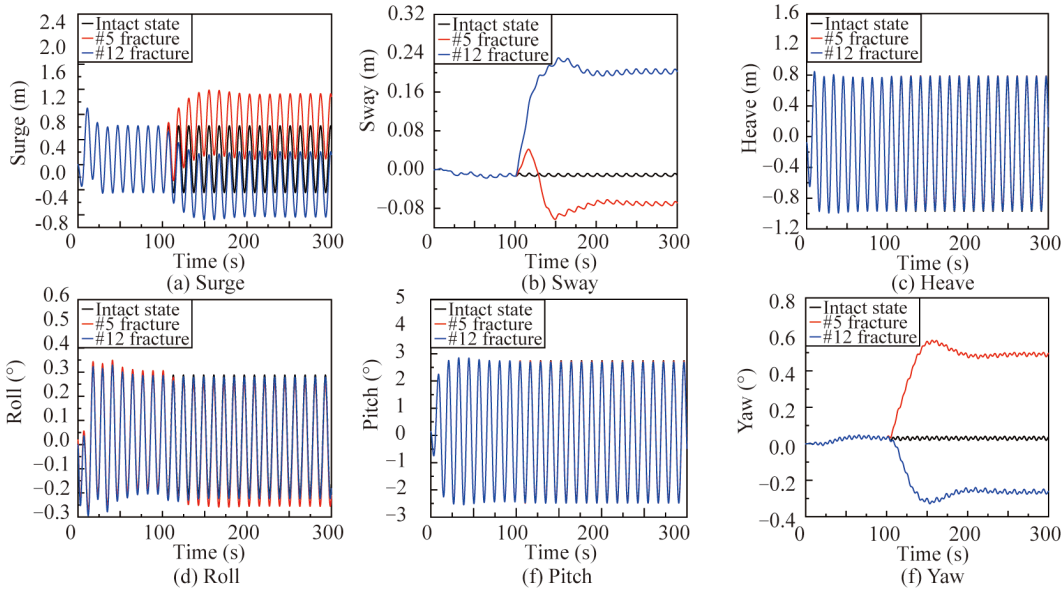

Fig. 9. Time history curves of M10 motions for three mooring scenarios under regular waves (12 s).

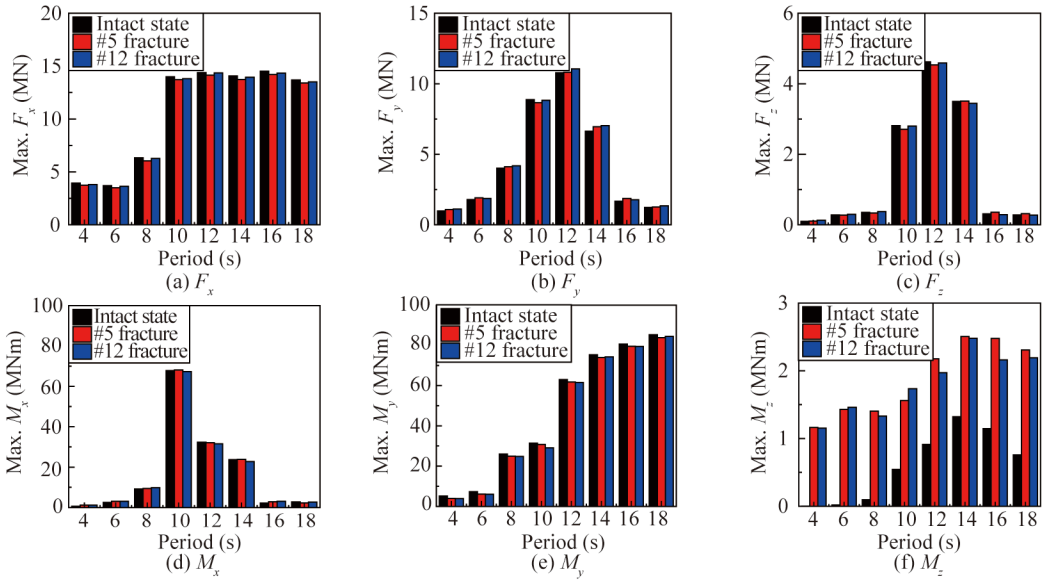

Fig. 10. Maximum connector loads of $C_{10,11}$ for three mooring scenarios under regular waves.

trends of connector loads along with the varying wave periods does not change at all when a single mooring line fractures. F_x, F_y, F_z, M_x, M_y and wave energy power all seem insensitive to a single mooring line fracture, which is due to the fact that the magnitude of certain connector loads (F_x, F_y, F_z, M_x, and M_y) is one or two orders higher than that of mooring line tensions, and the changes of those connector loads caused by mooring line fractures are extremely minor. However, M_z notably varies as it possesses the same magnitude as the mooring line tension.

4.2 Effects of one single mooring line fracture in the extreme sea condition

Hydrodynamic responses of the HMFS system under the extreme sea condition (H_s=4 m, T_p=10 s, λ=3.3, JONSWAP) (Wang et al., 2014) in three mooring scenarios (intact state, line #5 fracture, line #12 fracture) have been comparatively studied in this section. Maximum tensions of all mooring lines for three mooring scenarios are shown in Fig. 11. It can be seen intuitively that when the upstream-side mooring line #5 fractures, mooring tensions of the remaining upstream-side lines all increases. Similarly, the downstream-side line #12 fracture leads to tension increase in all remaining downstream-side lines. The force rebalance due to a single mooring line fracture is partly achieved by the increase of remaining mooring tensions on the same side. When the line #5 fractures, the maximum tension of its adjacent mooring line #4 has an increase of 66.05% and reaches 5.38 MN, which is the largest among all remaining mooring lines. Since the breaking strength of each mooring line is 8.50 MN, safety factor of line #4 is 1.58 which is smaller than the allowable safety factor of 1.67 mentioned in the referential specification API RP 2SK (American Petroleum Institute, 1996). In addition, the line #12 fracture leads to a maximum tension of 4.093 MN of adjacent mooring line #10, and the corresponding safety factor is 2.07, which is much larger than the allowable safety factor of 1.67. It implies that line #4 is at a risk of a progressive fracture following the fracture of upstream-side line #5, while the mooring system is relatively safe after the fracture of the downstream-side mooring line #12 in terms of mooring line breaking strength. Therefore, it is noted that measures should be taken swiftly for preventing a progressive mooring line fracture after the fracture of line #5.

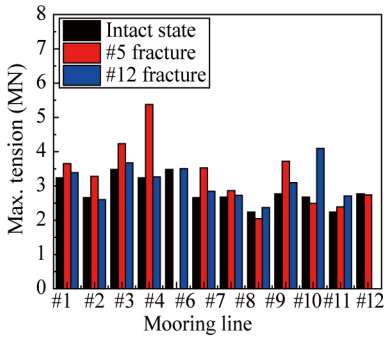

Fig. 11. Maximum mooring line tension for three mooring scenarios under the extreme wave condition.

Based on Section 4.1.2, heave, roll and pitch motions are all less sensitive to a single mooring line fracture. Therefore, only the maximum surge, sway and yaw of all inner semi-sub modules for three mooring scenarios under the extreme sea condition are presented in Fig. 12. The maximum surge, sway and yaw for all modules in two mooring fracture scenarios are both larger than those correspondingly in intact state. The fracture of upstream-side line #5 causes more growth in module motions (surge, sway and yaw) for all semi-sub modules than that of downstream-side line #12, which is because line #5 generally suffers larger mooring

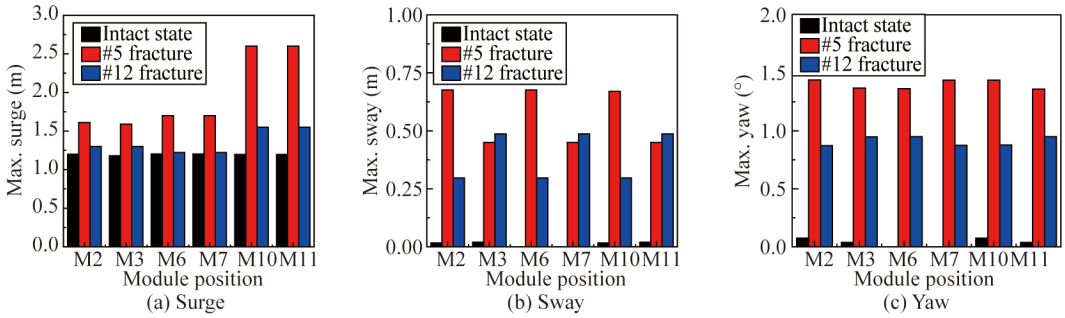

Fig. 12. Maximum module motions for three mooring scenarios under the extreme wave condition.

tension than line #12. Upstream-side semi-sub modules (M2, M6, M10) suffer larger sway growth in the scenario of line #5 fracture, while sway motions of downstream-side modules (M3, M7, M11) increase more significantly in the scenario of line #12 fracture. Maximum surge motions among all inner modules for the two fracture scenarios both occur in M10 and M11, which are 2.6 m and 1.55 m, respectively. Maximum sway motions among all inner modules for the two fracture scenarios are 0.67 m and 0.49 m, respectively. All semi-sub modules are in similar level in yaw motions for any given mooring scenarios, which is due to the relatively higher integrity of the HMFS system in yaw direction. Maximum yaw values for the two fracture scenarios are about 1.44° and 1.00°, respectively.

As mentioned in the referential specifications API RP 2SK (American Petroleum Institute, 1996), the maximum drift of platforms should not exceed 10% of the water depth in rough wave condition. Since the design water depth of the HMFS system in this paper is 40 m, the maximum safety drift is 4.0 m, which is larger than the maximum surge (2.6 m) and the maximum sway (0.67 m). Consequently, the HMFS system is relatively safe under the scenario of a single mooring line fracture in terms of module motions.

4.3 Effects of two mooring line fractures

The potential influence of a progressive fracture of a second mooring line on hydrodynamic responses of the HMFS system is comprehensively studied in this section. Since line #5 bears the maximum tension in intact state, it is regarded as the basis of two-line fracture cases. Four typical cases with two fractured mooring lines are selected for analysis (Table 5). Maximum tensions of the remaining mooring lines for four cases under the extreme sea condition (H_s= 4 m, T_p=10 s, λ=3.3, JONSWAP) (Wang et al., 2014) are shown in Fig. 13. In addition, results of line #5 fracture scenario are also provided for comparisons.

It can be seen that under the premise of line #5 fracture, the fracture of a second mooring line leads to significant tension increase of the other mooring lines in the same group. In Case 1, the maximum mooring tension occurs in line #6, and it increases sharply by 90.4%, from 3.53 MN to 6.72 MN. It is because line #6 undertakes the total mooring tension of its group alone after the successive fracture of lines #5 and #4. In other three cases, maximum tensions all appear in line #4. However, tension variations of line #4 for the three cases are all slight compared with that for mooring scenario of line #5 fracture. In addition, since the two fractured lines (#5 and #3) are symmetric with respect to *x*-axis, mooring line tensions are symmetrically the same for Case 4. The dashed line in Fig. 13 represents the calculated mooring line tension (5.08 MN) corresponding to the safe factor (1.67) mentioned in the referential specifications API RP 2SK. It can be obviously seen that maximum mooring tensions for four cases all exceed the maximum safe tension. Specifically, the mooring line tension (6.72 MN) of line #6 in Case 1 is substantially larger than the maximum safe tension (5.08 MN). Therefore, under the premise of line #5 fracture, line #4 or #6 is at a risk of a progressive fracture for all cases, especially line #6.

The maximum surge, sway and yaw of all inner semi-sub modules for four cases under the extreme sea condition are comparatively shown in Fig. 14. It indicates intuitively that the maximum motions of surge, heave and yaw all appear in Case 1 among all cases. Specifically, M10 which is connected to the two fractured mooring lines (#4 and #5) is of the largest surge motion (5.62 m) among all modules for Case 1. In addition, the maximum surge of M11 is similar to that of M10 due to their ball joint connection. Their surge motions dramatically exceed the maximum safety drift motion (4.0 m), leading to great harm to the stability and safety of the HMFS system. Therefore, it is of significance to prevent fractures of two mooring lines from occurring in the same group. For Case 1, the maximum sway of M11 (2.58 m) is the largest among all semi-sub modules, which

Table 5 Four representative cases for two mooring line fracture

Case number	Case 1	Case 2	Case 3	Case 4
Fractured mooring lines	#5 and #4 (same group)	#5 and #12 (opposite side)	#5 and #9 (diagonal side)	#5 and #3 (same side)

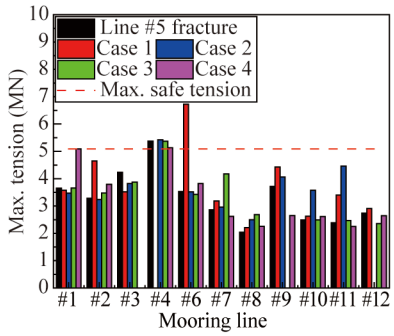

Fig. 13. Mooring tension distributions for four cases under extreme sea condition.

is within the safety range. The yaw of all semi-sub modules is similar, being about 4°. For Case 2 and Case 3, M10 and M11 are in similar surge motions of 2.7 m which is smaller than the maximum safety drift (4.0 m). All modules are in similar sway in Case 2 or Case 3, and they are both within the safe drift range. For Case 4, since the mooring system is symmetric with respect to *x*-axis, it presents certain characteristics similar to those in intact state. All modules are in the similar surge value of 2.17 m, while it is almost doubled compared with the corresponding value in static state (1.2 m). In addition, the sway and yaw are both quite small and even close to zero.

Fig. 15 presents the horizontal-plane trace of the representative modules (M10 and M11) for four cases under the extreme sea condition. The surge and sway range of M10 and M11 in Case 1 are obviously larger than those correspondingly in other three cases. The traces of M10 and M11 in Case 4 both present line segments, which are almost parallel to the *x*-axis and passing through their initial gravity center point (−22, −44) and (22, −44), respectively. It indicates that the module sway motion is insensitive to mooring scenarios like Case 4.

Based on Section 4.1.3, F_x, F_y, F_z, M_x, and M_y are all insensitive to mooring line fractures. Therefore, Fig. 16 only presents the maximum M_z of the representative connector $C_{10,11}$ for different cases under the extreme sea condition. It can be seen that M_z of $C_{10,11}$ in Case 1 is almost triple the value in intact state and reaches 11.65 MNm, which is exceedingly larger than those in other cases. The maximum M_z of $C_{10,11}$ for intact state and Case 4 are similar, which is because the mooring line system of Case 4 remains symmetric about the *x*-axis.

It is noted that Case 1 is the most harmful among all four cases in consideration of mooring line tensions, module motions and connector loads. Therefore, effective measures must be timely taken to prevent the adjacent mooring line from a progressive fracture.

4.4 Effects of relaxing proper mooring lines

As noted in Section 4.3, it is extremely dangerous for a progressive fracture in the adjacent line #4 after the fracture of line #5. Therefore, it is significant to take measures to

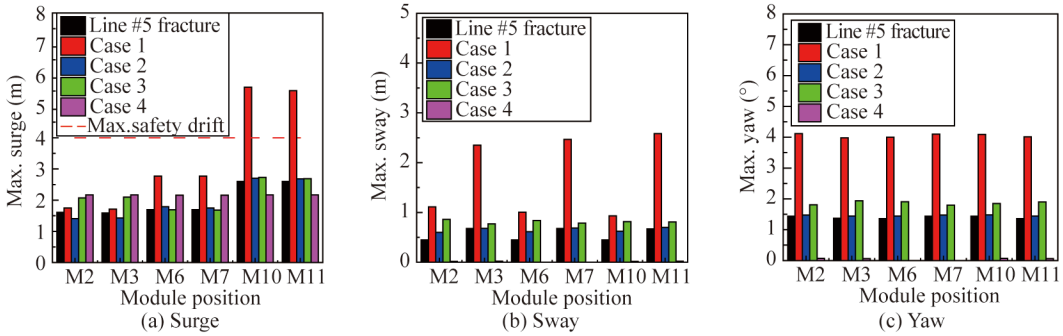

Fig. 14. Maximum module motions for four cases under the extreme wave condition.

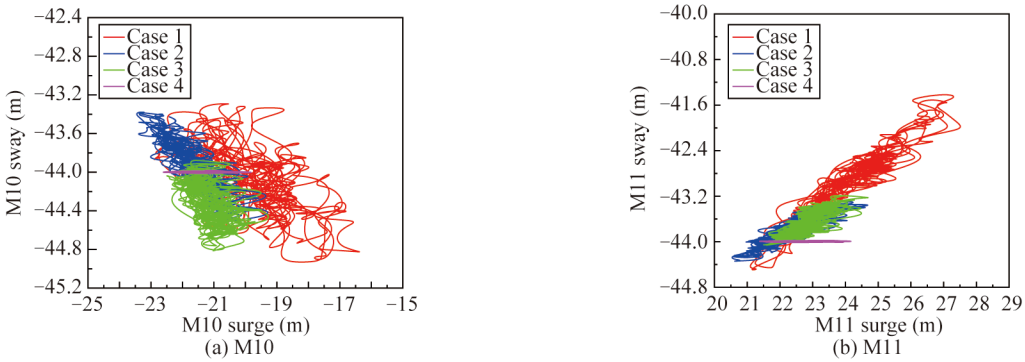

Fig. 15. Horizontal plane traces of M10 and M11 for four cases under extreme wave condition.

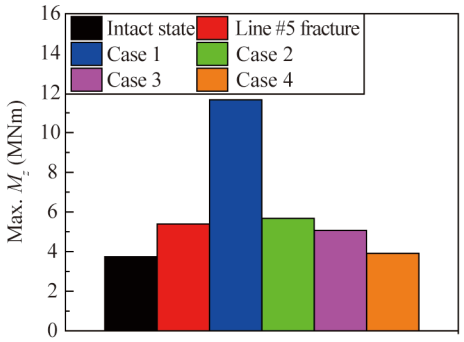

Fig. 16. Maximum M_z of $C_{10,11}$ for different cases under the extreme wave condition.

reduce the maximum mooring line tension (5.376 MN) of line #4 to a level below the maximum safe tension (5.08 MN). Since the increase of mooring line relaxation may lead to the decrease in mooring line tension and growth in module motions to some extent (Shafieefar and Rezvani, 2007), it is considered to appropriately lengthen the mooring line #4 to increase the angle between the catenary line and the water surface for larger relaxation. When the sudden fracture of line #5 occurs, line #4 is lengthened by 5 m timely.

The scenario of single line #5 fracture is named as Case A, and the scenario of line #4 relaxation after line #5 fracture is named as Case B. Fig. 17 presents the maximum mooring line tensions and module motions for Case A and Case B under the extreme sea condition. In Fig. 17a, it can be seen that maximum tensions of all remaining mooring lines in Case B are lower than the maximum safe tension (5.08 MN) shown as the red dash line. Specifically, the tension of line #4 reduces from 5.38 MN to 4.49 MN, while the tension of line #6 increases from 3.53 MN to 4.76 MN. The other mooring lines, except lines #4 and #6, suffer slight changes in tension after line #4 relaxation. In Fig. 17b, surge motions of all semi-sub modules increase to varying degrees mainly due to the weakened constraints caused by the relaxation of mooring line #4. It is noted that the maximum surge motions of M10 and M11 both reach 2.99 m which is within the safety range. Therefore, it can be inferred that the emergency strategy with appropriate relaxation of a proper mooring line is effective to reduce the risk of more progressive mooring line fractures.

4.5 Effects of connector failures

Since the wave incident angle is 0°, significant M_y of certain outermost connectors may bring damages to the hydraulic PTO unit and even lead to a case that the PTO damping coefficient (K_p) changes to be zero in extremis. Similarly, certain inner connectors bear large pitch torques, which may cause pitch spring damage and even lead to an extremely sharp decrease of pitch spring stiffness coefficient (K_s) to be zero. With the symmetry of the HMFS system, the maximum M_y of $C_{5,6}$ (136.45 MNm) is larger than that of $C_{9,10}$ (123.51 MNm), and the maximum M_y of $C_{6,7}$ (157.11 MNm) is larger than that of $C_{10,11}$ (138.81 MNm). Therefore, it can be preliminarily considered that the connector failures more likely occur to $C_{5,6}$ among outermost connectors and to $C_{6,7}$ among inner connectors. Specifically, the failure of the pitch PTO damping system of $C_{5,6}$ (K_p= 0 NMs/rad) and the failure of pitch spring system of $C_{6,7}$ (K_s (pitch)=0 Nm/rad) are primarily considered for investigating the influence of connector failures on hydrodynamic performance of the HMFS system.

Fig. 18 presents the main maximum module motions (surge, heave and pitch) of representative modules (M5, M6, M7, M9, M10, M11) for three connector scenarios(intact state, $C_{5,6}$ failure, $C_{6,7}$ failure) under the extreme sea condition (H_s=4 m, T_p=10 s, λ=3.3, JONSWAP). It can be seen that surge motions for all modules are insensitive to connector failures. It may because the surge motion is related to wave force and stressed area in surge direction, while connector failures have little effect on the two factors. When the outermost connector $C_{5,6}$ suffers a failure (K_p=0 NMs/rad), the modules (M5, M6 and M7) in the same row with $C_{5,6}$ all show significant increase in heave and pitch, especially the adjacent outermost module M5. However, heave and pitch motions of modules (M9, M10, M11) in a different row with $C_{5,6}$ almost remain unchanged. When the failure occurs on the inner connector $C_{6,7}$ (K_s (pitch)= 0 Nm/rad), modules (M5, M6 and M7) all increase in heave and pitch, and the

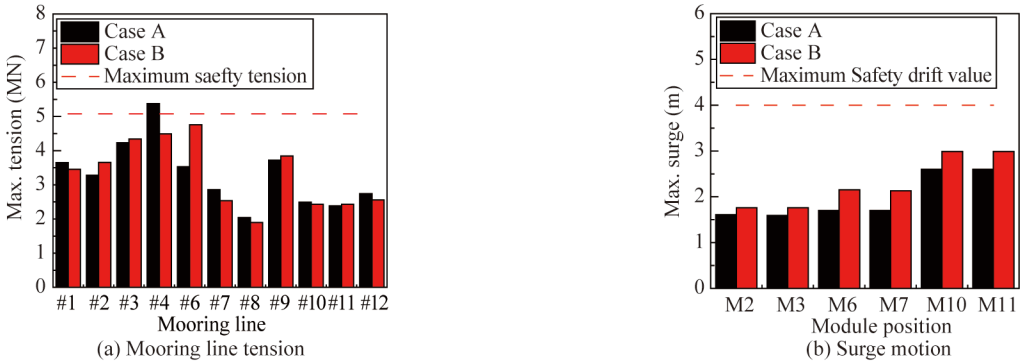

Fig. 17. Maximum mooring tensions and surge motions in Case A and Case B under the extreme sea condition.

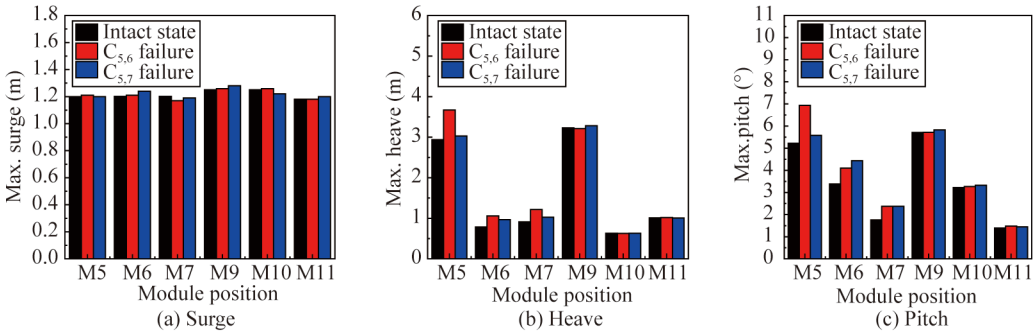

Fig. 18. Maximum module motions for three connector scenarios under the extreme sea condition.

adjacent inner module M6 suffers the largest growth. The other modules all change slightly in heave and pitch. Therefore, it can be inferred that the main module motions (surge, heave, pitch) are less sensitive to failures of connectors in other rows, and the reason may be that the ball joints release relative rotations between longitudinal adjacent inner modules. In addition, failures of outermost connectors exert more significant influence on module motions, which may be due to that PTO damping systems of outermost connectors are of effectiveness in reduction of module motions (Liu et al., 2021).

Fig. 19 presents the main maximum connector loads (F_x, F_z and M_y) of representative connectors ($C_{5,6}$, $C_{6,7}$, $C_{9,10}$, $C_{10,11}$) for three connector scenarios (intact state, $C_{5,6}$ failure, $C_{6,7}$ failure) under the extreme sea condition. In general, F_x for all connectors are less sensitive to connector failures. It is because F_x is related to relative surge of adjacent modules, and the module surge almost stay unchanged with a connector failure. When connector failures occur in the connectors $C_{5,6}$ and $C_{6,7}$, F_z values of $C_{5,6}$ obviously increase while those of $C_{6,7}$ reduce, which may be due to the reason that $C_{5,6}$ failure leads to a larger relative heave to adjacent modules. However, $C_{9,10}$ and $C_{10,11}$, both are in different row with the failed connector, show extremely slight changes in F_z because of heave insensitivities of M9 and M10 to the failures of the connector $C_{5,6}$ and $C_{6,7}$. M_y of $C_{5,6}$ decreases after the failure of $C_{6,7}$, and M_y of $C_{6,7}$ decreases after the failure of $C_{5,6}$. However, $C_{9,10}$ and $C_{10,11}$ in different row with failed connectors ($C_{5,6}$ and $C_{6,7}$) show relatively slight variations in M_y due to smaller changes of relative pitch.

Fig. 20 presents the influence of connector failures ($C_{5,6}$ and $C_{6,7}$) on mooring line tensions. It can be seen that $C_{5,6}$ failure leads to a slight increase in tensions for all mooring lines, while mooring line tensions almost stay unchanged after the failure of $C_{6,7}$. It is becasue the PTO damping systems can reduce the incident wave energy to a certain extent. In addition, since the change of mooring line tension is directly related to the variation of horizontal plane motions (surge, sway) of the fairlead point, the horizontal plain traces of the fairlead point in M10 for three connector scenarios are presented in Fig. 21. It shows slight changes in drift trajectory when connector failures occur, which further indicates that mooring line tensions are generally less sensitive to failures of certain connectors.

5 Conclusions

This work focuses on effects of both mooring line fractures and connector failures on hydrodynamic performances of a Hybrid Modular Floating Structure (HMFS) system. In addition, one emergency strategy of increasing the relaxation of proper mooring lines to reduce the risk of more progressive mooring line fractures has been proposed and analyzed. Main conclusions can be drawn as follows.

(1) When one single mooring line fracture occurs, the maximum tension appears in its adjacent mooring line. In addition, the minimum tension appears in the opposite side of the fractured mooring line, and corresponding locations changes with different wave periods.

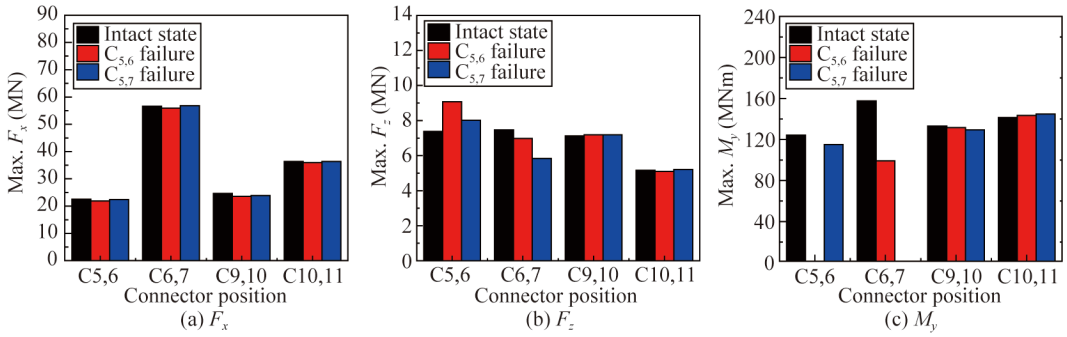

Fig. 19. Maximum connector loads for three connector scenarios under the extreme sea condition.

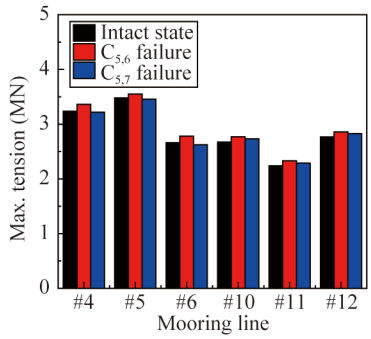

Fig. 20. Maximum mooring line tensions for three connector scenarios under the extreme sea condition.

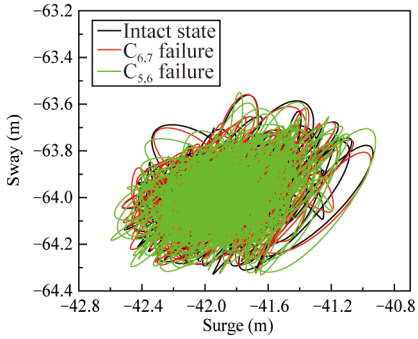

Fig. 21. Horizontal plane traces of the fairlead point on M10 for three connector scenarios under the extreme sea condition.

(2) For module motions, equilibrium positions of horizontal plane motions (surge, sway and yaw) of all modules vary significantly after one single mooring line fracture, and fractured mooring lines on both up-stream side and down-stream side make modules to drift to new equilibrium positions along reverse directions. The maximum surge always appears in the module connected to the fractured mooring line. However, equilibrium positions of the other motion responses (heave, roll, pitch) are less sensitive to one single mooring line fracture. For connector loads, M_z changes obviously with the fracture of one single mooring line, while the other connector loads (F_x, F_y, F_z, M_x and M_y) are less sensitive to that.

(3) For the extreme sea condition, when the mooring line with the maximum tension suffers a failure, the maximum tension of its adjacent mooring line significantly increases, which is larger than its maximum safe level. In addition, the case with two fractured mooring lines in the same group on the upstream side is the most dangerous among all cases of two-line failures in view of mooring line tensions, module motions and connector loads. Therefore, effective measures should be timely taken to prevent the adjacent mooring line from a progressive fracture. One proposed emergency strategy of appropriate relaxation of the mooring line adjoining the existing fractured line is effective to reduce the risk of progressive mooring line fractures.

(4) The surge of modules, F_x of connectors and the mooring line tensions are less sensitive to connector failures. Module motions (heave and pitch) and corresponding connectors loads (F_z and M_y) in the same row with failed connectors all change significantly, while those in different rows with the failed connector change slightly.

References

Ahmed, M.O., Yenduri, A. and Kurian, V.J., 2016. Evaluation of the dynamic responses of truss spar platforms for various mooring configurations with damaged lines, *Ocean Engineering*, 123, 411–421.

American Petroleum Institute, 1996. *Recommended Practice for Design and Analysis of Stationkeeping Systems for Floating Structures*, American Petroleum Institute, Washington.

Bae, Y.H., Kim, M.H. and Kim, H.C., 2017. Performance changes of a floating offshore wind turbine with broken mooring line, *Renewable Energy*, 101, 364–375.

Berstad, A.J., Tronstad, H. and Ytterland, A., 2004. Design rules for marine fish farms in Norway: calculation of the structural response of such flexible structures to verify structural integrity, *ASME 2004 23rd International Conference on Offshore Mechanics and Arctic Engineering*, ASMEDC, Vancouver, pp. 867–874.

Chen, M.S., Guo, H.R., Wang, R., Tao, R. and Cheng, N., 2021. Effects of gap resonance on the hydrodynamics and dynamics of a multi-module floating system with narrow gaps, *Journal of Marine Science and Engineering*, 9(11), 1256.

Cheng, H., Li, L., Ong, M.C., Aarsæther, K.G. and Sim, J., 2021. Effects of mooring line breakage on dynamic responses of grid moored fish farms under pure current conditions, *Ocean Engineering*, 237, 109638.

Cheng, Y., Xi, C., Dai, S.S., Ji, C.Y., Collu, M., Li, M.X., Yuan, Z.M. and Incecik, A., 2022. Wave Energy extraction and hydroelastic response reduction of modular floating breakwaters as array wave energy converters integrated into a very large floating structure, *Applied Energy*, 306, 117953.

Chuyen, P.D., 2009. *Innovative Solutions for Minimizing Differential Deflection and Heaving Motion in Very Large Floating Structures*, Ph.D. Thesis, National University of Singapore, Singapore.

Cummins, W.E., 1962. *The Impulse Response Function and Ship Motions*, David Taylor Model Basin, Washington.

Du, S.X. and Ertekin, C.R., 1991. Dynamic response analysis of a flexibly joined, multi-module Very Large Floating structure, *OCEANS*

91 Proceedings, IEEE, Honololu, pp. 1286–1293.

Faltinsen, O.M., 1990. *Sea Loads on Ships and Offshore Structures*, Cambridge University Press, Cambridge.

Fontaine, E., Kilner, A., Carra, C., Washington, D., Ma, K.T., Phadke, A., Laskowski, D. and Kusinski, G., 2014. Industry survey of past failures, pre-emptive replacements and reported degradations for mooring systems of floating production units, *Proceedings of the Offshore Technology Conference*, OTC, Houston, pp. 5–8.

Jung, K., Lee, S., Kim, H., Choi, Y. and Kang, S., 2020. Design and construction of the floating concrete pier in golden harbor, Incheon, in: Wang, C.M., Lim, S.H. and Tay, Z.Y. (eds.), *WCFS2019*, Springer, Singapore, pp. 283–297.

Kim, B.W., Hong, S.Y., Kyoung, J.H. and Cho, S.K., 2007. Evaluation of bending moments and shear forces at unit connections of very large floating structures using hydroelastic and rigid body analyses, *Ocean Engineering*, 34(11–12), 1668–1679.

Kim, B.W., Sung, H.G., Hong, S.Y. and Hong, S.W., 2014. Dynamic coupled analysis of FSRU with broken mooring line, *Proceedings of the Twenty-Fourth International Ocean and Polar Engineering Conference*, ISOPE, Busan, pp. 15–20.

Li, Y., Zhu, Q., Liu, L.Q. and Tang, Y.G., 2018. Transient response of a SPAR-type floating offshore wind turbine with fractured mooring lines, *Renewable Energy*, 122, 576–588.

Li, Y.W., Ren, N.X., Li, X. and Ou, J.P., 2022. Hydrodynamic Analysis of a novel modular floating structure system integrated with floating artificial reefs and wave energy converters, *Journal of Marine Science and Engineering*, 10, 1091.

Lian, Y.S., Yim, S.C., Zheng, J.H., Liu, H.X. and Zhang, N., 2020. Effects of damaged fiber ropes on the performance of a hybrid taut-wire mooring system, *Journal of Offshore Mechanics and Arctic Engineering*, 142(1), 011607.

Lian, Y.S., Zheng, J.H., Liu, H.X., Xu, P.F. and Gan, L.L., 2018. A study of the creep-rupture behavior of HMPE ropes using viscoelastic-viscoplastic-viscodamage modeling, *Ocean Engineering*, 162, 43–54.

Liu, Y.Q., Ren, N.X. and Ou, J.P., 2021. Hydrodynamic analysis of a hybrid modular floating structure system and its expansibility, *Ships and Offshore Structures*, doi: 10.1080/17445302.2021.1996110.

Liu, Y.Q., Ren, N.X. and Ou, J.P., 2022. Hydrodynamic analysis of a hybrid modular floating structure system under different wave directions, *Applied Ocean Research*, 126, 103264.

Ma, G., Zhong, L., Zhang, X., Ma, Q.W. and Kang, H.S., 2020. Mechanism of mooring line breakage of floating offshore wind turbine under extreme coherent gust with direction change condition, *Journal of Marine Science and Technology*, 25(4), 1283–1295.

Ma, K.T., Shu, H.B., Smedley, P., L'Hostis, D. and Duggal, A., 2013. A Historical review on integrity issues of permanent mooring systems, *Offshore Technology Conference*, Houston, 24025.

Malayjerdi, E., Ahmadi, A. and Tabeshpour, M.R., 2016. Dynamic Analysis of TLP in intact and damaged tendon conditions, *The 18th Marine Industries Conference* (*MIC2016*), Kish Island.

Manabe, H., Uehiro, T., Utiyama, M., Esaki, H., Kinoshita, T., Takagi, K., Okamura, H. and Satou, M., 2008. Development of the floating structure for the sailing-type offshore wind farm, *OCEANS 2008 - MTS/IEEE Kobe Techno-Ocean*, IEEE, Kobe, pp. 1–4.

Miao, G.P., Ishida, H. and Saitoh, T., 2000. Influence of gaps between multiple floating bodies on wave forces, *China Ocean Engineering*, 14(4), 407–422.

Newmark, N.M., 1959. A method of computation for structural dynamics, *Journal of the Engineering Mechanics Division*, 85(3), 67–94.

Nguyen, H.P., Wang, C.M., Tay, Z.Y. and Luong, V.H., 2020. Wave energy converter and large floating platform integration: a review, *Ocean Engineering*, 213, 107768.

Qiao, D.S., Li, B.B., Yan, J., Qin, Y., Liang, H.Z. and Ning, D.Z., 2021. Transient responses evaluation of FPSO with different failure scenarios of mooring lines, *Journal of Marine Science and Engineering*, 9(2), 103.

Ren, N.X., Wu, H.B., Ma, Z. and Ou, J.P., 2020. Hydrodynamic analysis of a novel modular floating structure system with central tension-leg platforms, *Ships and Offshore Structure*, 15(9), 1011–1022.

Ren, Y.J., Venugopal, V. and Shi, W., 2022. Dynamic analysis of a multi-column TLP floating offshore wind turbine with tendon failure scenarios, *Ocean Engineering*, 245, 110472.

Shafieefar, M. and Rezvani, A., 2007. Mooring optimization of floating platforms using a genetic algorithm, *Ocean Engineering*, 34(10), 1413–1421.

Suzuki, H., 2005. Overview of Megafloat: concept, design criteria, analysis, and design, *Marine Structures*, 18(2), 111–132.

Wang, C.M. and Tay, Z.Y., 2011. Very large floating structures: applications, research and development, *Procedia Engineering*, 14, 62–72.

Wang, C.M. and Wang, B.T., 2015. *Large Floating Structures: Technological Advances*, Springer, Singapore.

Wang, Y.T., Xu, S.W., Wang, L. and Wang, X.F., 2019. Motion responses of a catenary–taut–tendon hybrid moored single module of a semisubmersible-type VLFS over uneven seabed, *Journal of Marine Science and Technology*, 24(3), 780–798.

Wang, Z.F., Zhou, L.M., Dong, S., Wu, L.Y., Li, Z.B., Mou, L. and Wang, A.F., 2014. Wind wave characteristics and engineering environment of the South China sea, *Journal of Ocean University of China*, 13(6), 893–900.

Yang, Y., Bashir, M., Li, C. and Wang, J., 2021. Investigation on mooring breakage effects of a 5 MW barge-type floating offshore wind turbine using F2A, *Ocean Engineering*, 233, 108887.